Author/s:
Wen, D;Pan, K;Meng, J;Wu, X;Guo, X;Li, P;Liu, S;Li, D;Wei, B;Xie, X;Yang, D;Zhao, J;Crozier, KB

Title:
Broadband Multichannel Cylindrical Vector Beam Generation by a Single Metasurface

Date:
2022-10-01

Citation:
Wen, D., Pan, K., Meng, J., Wu, X., Guo, X., Li, P., Liu, S., Li, D., Wei, B., Xie, X., Yang, D., Zhao, J. & Crozier, K. B. (2022). Broadband Multichannel Cylindrical Vector Beam Generation by a Single Metasurface. Laser and Photonics Reviews, 16 (10), https://doi.org/10.1002/lpor.202200206.

Broadband Multichannel Cylindrical Vector Beam Generation by a Single Metasurface

Dandan Wen, Kai Pan, Jiajun Meng, Xuanguang Wu, Xuyue Guo, Peng Li, Sheng Liu, Dong Li, Bingyan Wei, Xin Xie, Dexing Yang, Jianlin Zhao and Kenneth B. Crozier**

D. Wen, K. Pan, X. Wu, X. Guo, P. Li, S. Liu, D. Li, B. Wei, X. Xie, D. Yang, J. Zhao
Key Laboratory of Light Field Manipulation and Information Acquisition, Ministry of Industry and Information Technology, and Shaanxi Key Laboratory of Optical Information Technology, School of Physical Science and Technology, Northwestern Polytechnical University, Xi'an 710129, China
E-mail: jlzhao@nwpu.edu.cn

D. Wen, J. Meng, K. B. Crozier
Department of Electrical and Electronic Engineering, University of Melbourne, Victoria 3010, Australia

J. Meng, K. B. Crozier
School of Physics, University of Melbourne, Victoria 3010, Australia
Australian Research Council (ARC) Centre of Excellence for Transformative Meta-Optical Systems, University of Melbourne, Victoria 3010, Australia
E-mail: kcrozier@unimelb.edu.au

Keywords: metasurfaces, multichannel, cylindrical vector beam, broadband, high order Poincaré sphere

Abstract

Beams with spatially-varying polarization states have been the topic of much interest recently due to the unusual ways in which they can interact with matter. Cylindrical vector beams (CVBs) represent the most commonly used type and feature cylindrically-symmetric polarization distributions. The optical systems employed thus far for their generation have usually only been able to produce a single CVB. To generate and observe multiple CVBs,

bulky optical systems with stringent alignment tolerances have been needed. Here, we demonstrate a method to generate an array of CVBs using a single optical element, namely a transmission-mode dielectric metasurface. The incident light is split into an array of left and right-handed circularly polarized vortex beams that superpose with a controllable phase difference. We experimentally demonstrate an array of CVBs with 12 channels over a broad wavelength range. Our method produces a significant increase in the number of polarization channels compared to previous reports and solves the long-standing challenge of unequal intensity distributions. We furthermore improve the flexibility of the vector field control by not only generating CVBs of different orders but also controlling their polarization rotation. Our method may pave the way for applications in optical communications, laser machining, and optical trapping.

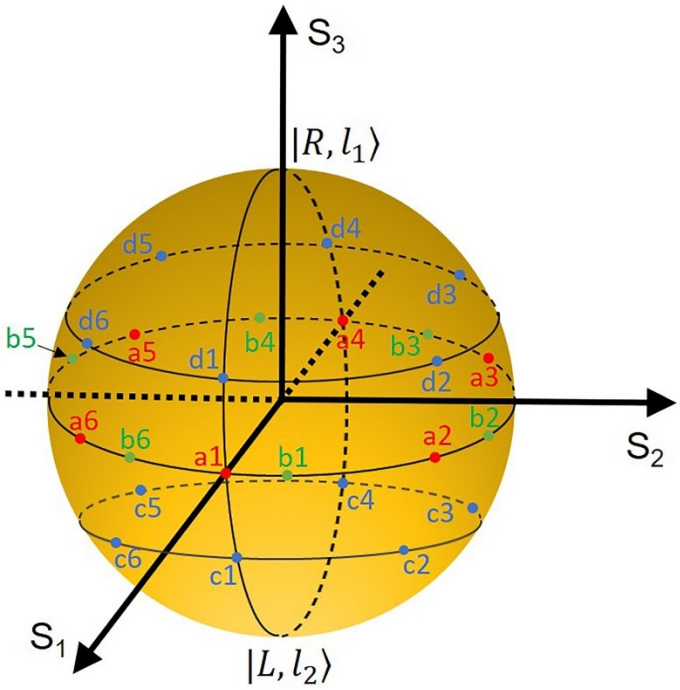

A method to generate an array of cylindrical vector beams (CVBs) using a single transmission-mode dielectric metasurface is proposed. An array of CVBs with 12 channels over a broad wavelength range is demonstrated. The method produces a significant increase in the number of polarization channels compared to previous reports and solves the long-standing challenge of unequal intensity distributions.

1. Introduction

Cylindrical vector beams (CVBs) represent solutions of Maxwell's equations that have axial symmetry in both amplitude and phase[1]. Unlike a Gaussian beam or a plane wave with a spatially homogeneous state of polarization, a CVB has a cylindrically symmetric polarization distribution over its cross section. Its intensity distribution is doughnut-like, due to the polarization singularity in the center. Due to their unique polarization distributions, CVBs have found applications that include plasmon excitation[2], imaging[3], optical trapping[4], laser machining[5] and so on[6]. Methods for CVB generation employed thus far can be broadly categorized as active and passive methods. The former usually involve the use of an axially-birefringent component (e.g. calcite crystal with its crystal axis along the propagation direction of light) in a laser cavity[7]. Such a cavity provides discrimination for the cylindrical modes, i.e. over the fundamental mode. This forces the system to oscillate in the cylindrical mode. Passive methods generally use devices with spatially-varying polarization properties (such as spatial light modulators, SLMs) to convert homogeneous polarizations into CV polarizations[8-9], or use few-mode fibers whose TE_{01} and TM_{01} modes are azimuthally- and radially-polarized, respectively[10].

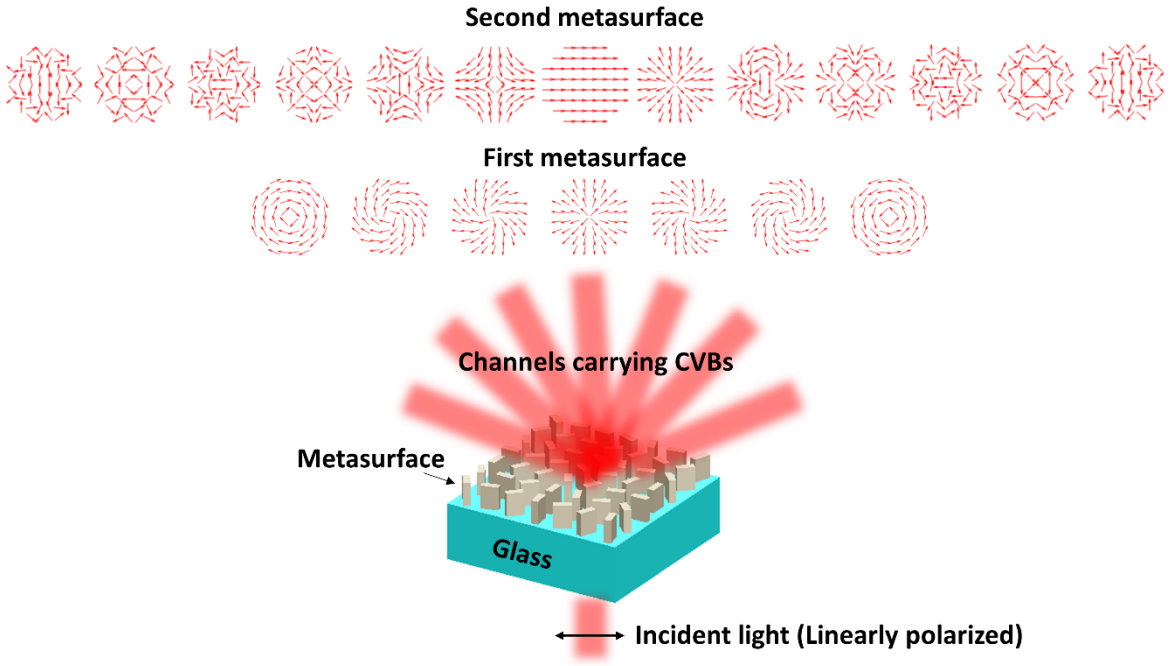

Figure 1 Schematic illustration of metasurface-based CVBs generation. Incident beam illuminates amorphous silicon (a-Si) metasurface on glass substrate. Transmitted light contains different CVBs, e.g. on different diffraction orders. Two metasurface types are demonstrated in this work. In the first, seven CVB channels of the same order are generated. In the second, there are 13 diffraction orders in total. The 0^{th} order is linearly polarized, however. This means that only 12 CVBs are produced.

The active and passive methods described above each generally produce one CVB type at a time. As noted above, there is growing interest concerning systems that can simultaneously generate multiple CVBs. Such devices could benefit many applications. They could for example enable the number of channels to be boosted in vector beam-based, high speed free-space optical communication systems[11]. Similarly, for low power optical trapping systems with vector beams, the number of trapping channels could be increased without additional optical elements[4]. In recent years, researchers have expended much effort on the development of such systems. In 2017, Rosales-Guzmán et al[12] used an SLM to split an incident beam into many orders, modulate its phase, amplitude and shape, and then recombine the orders with an optical system, thereby generating multiple vector beams. Tang et al[13] also used an SLM to split the incident light. An azimuthally-varying geometric phase element was placed at the image plane of the SLM in a 4-*f* system. The different diffraction orders then passed through the center of the phase element and were transformed into vector vortex beams of the same order. Although these works successfully demonstrated the generation of multiple vector beams, they were implemented in systems with large footprints. This was because they were traditional optical systems employing bulk optical components such as beam splitters, waveplates, and lenses.

The past decade has witnessed fast progress in metasurface development[14-26], which has resulted in researchers investigating the generation of CVBs with metasurfaces[27-36]. However, most works have been single channel devices, or multiple channels carrying the same CVB. Here we briefly review recent works on metasurface-based multichannel CVB generation. Yue et al[37] proposed a multi-channel, angular multiplexing CVB generation method. Four vortex beams with different topological charges were realized in separate channels with a single reflective-type plasmonic metasurface. Wang et al[38] used a metalens to generate LCP and RCP focused OAM beam arrays that in turn produced multiple focused CVBs when recombined. While these two works successfully demonstrate CVB array

generation, only four channels are realized since only the phase functions of the complex OAM hologram are used, which leads to uneven power distribution among the channels when further increasing the channel number[39]. Jiang et al[39] used multi-layered metasurfaces to simultaneously control the complex amplitude of the LCP and RCP components. When recombined, these form the CVB array. This demonstration however was performed at microwave frequencies because the complexity of the unit cell made fabrication infeasible for visible or infrared operation.

Here, we demonstrate the generation of multiple CVBs with a single dielectric metasurface. This avoids the need for bulky optical systems with stringent alignment tolerances and provides unique advantages in comparison with previous works. The metasurface generates LCP and RCP vortex beam arrays. These recombine to form multiple CVBs with different polarization distributions (Figure 1). This approach makes use of the diffraction direction-related phase difference between the LCP and RCP vortex beams, i.e. the desired CVBs are produced via appropriate choice of the propagation directions of the different orders. The number of CVBs generated is determined by the Dammann grating factor within the phase profile of the metasurface. This can be extended at will and solves the problems of limited channels and unequal power distributions of the previous works. The geometric phase we use here, as well as the phase difference between the RCP and LCP vortex beams at a given order, are all wavelength-independent, which makes the metasurface applicable for a broad wavelength range. In addition, this approach provides much flexibility on how to control vector fields because it allows us to not only generate CVBs of different orders but also to control their polarization rotation. Our metasurfaces comprise a-Si on glass, which can be fabricated through standard deposition, lithography and processes, making them suitable for numerous of applications at visible and near infrared wavelengths.

2. Results

Here we use transmission-type geometric metasurfaces as schematically shown in Figures 1 and 2a. Each metasurface comprises a-Si nanopillars on a glass substrate. Each nanopillar can be regarded as an anisotropic scatterer that modulates the complex amplitude of the transmitted light along its long and short axes differently. As result, when a nanopillar is illuminated by RCP (LCP) incident light, part of the transmitted light has helicity opposite to that of the incident light, i.e., to LCP (RCP), and carries geometric phases of $+2\theta(-2\theta)$, where θ represents the orientation of the nanopillar. One can therefore readily encode a desired

phase profile in an array of nanopillars, each having the same geometry but with a different orientation.

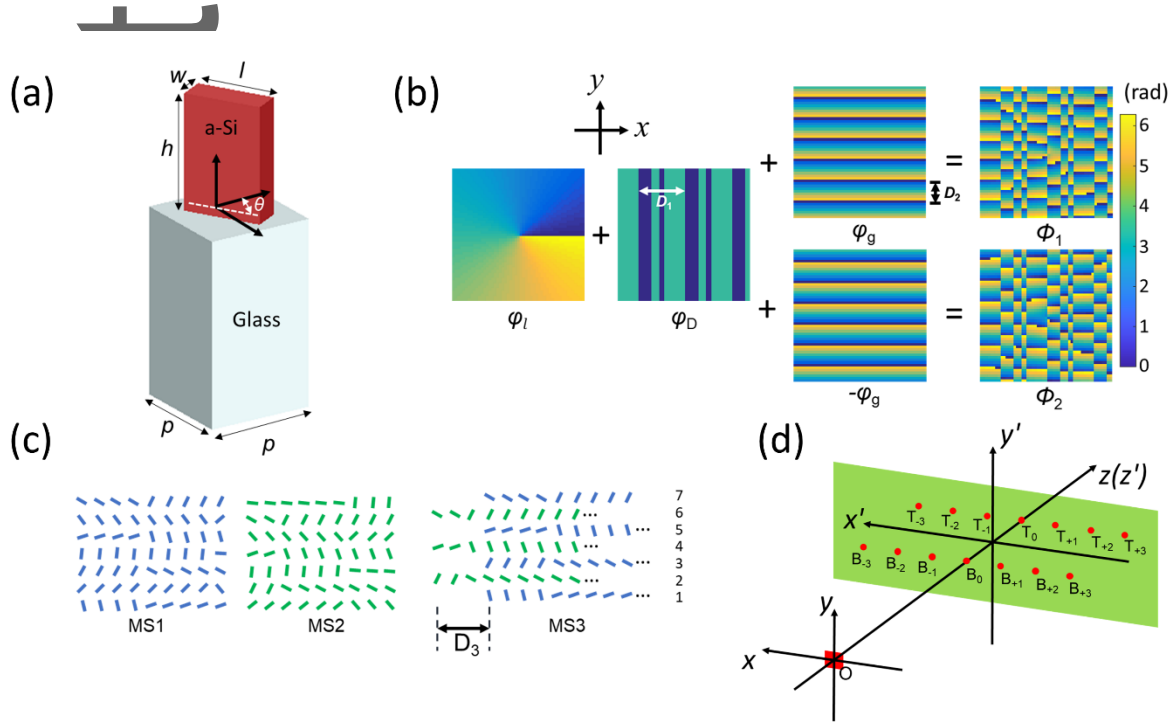

Figure 2 Schematic illustration of CVB generation with metasurface. (a) Schematic of metasurface unit cell, comprising a-Si nanopillar (height h) on glass substrate. Nanopillars are arranged in a square lattice (lattice constant p). Width, length and orientation of nanopillar are denoted by w, l and θ, respectively. (b) Schematic illustration of process by which phase profiles Φ_1 and Φ_2 are generated. (c) Φ_1 and Φ_2 are encoded onto geometric metasurfaces MS1 and MS2, respectively, which are then interleaved to form MS3. (d) Schematic of diffraction orders that carry CVBs. T_{-3} to T_{+3} represent the -3 to +3 diffraction orders on the **top** half of the observation plane. Similarly, B_{-3} to B_{+3} represent the orders on the **bottom** half of the observation plane.

The design principle for our metasurface is as follows. As shown in Figure 2b, the phase profile of Φ_1 is chosen to be as follows:

$$\Phi_1 = \varphi_l + \varphi_D + \varphi_g \quad (1)$$

Where φ_l is a spiral phase profile with a topological charge of l. φ_D denotes the phase profile of a Dammann grating, which splits and diverts the incident light to the desired diffraction orders with certain intensity distribution. Dammann gratings are phase-only gratings, i.e., they are transparent and provide negligible amplitude modulation. There are only two phase values within each period. The phase distribution is determined by the function that the

grating is designed for, such as the number of diffraction orders and the power distribution among them. As shown in Figure 2b, we have two phase steps of 0 and π within each period D_1. Typically, a Dammann grating is fabricated by etching a transparent dielectric substrate, where the etch depth controls the phase value. Rather than doing this, we here control the phase value via the concept of geometric phase. Details concerning the Dammann grating design are given in Supplementary Note 1. φ_g provides a phase gradient along the y-direction, with the phase varying linearly from 0 to 2π within a period D_2.

The phase profile Φ_1 is encoded onto the geometric metasurface MS1 (Figure 2c, blue color). When the incident light is RCP, the LCP light transmitted by MS1 will carry the geometric phase profile Φ_1. Due to synergy between the three terms comprising Φ_1 in Equation (1), an array of LCP OAM beams is generated with a topological charge of l (here denoted as $|L, l\rangle$) and deflected to the $\mathbf{T_{-3}} \sim \mathbf{T_{+3}}$ orders as shown in Figure 2d, where for illustration purposes we show seven orders. The relationship between propagation directions of these orders and the values of (D_1, D_2) is given in Supplementary Note 2. When the incident light is LCP, the phase profile of the RCP light transmitted by MS1 is $-\Phi_1$ due to the inherent property of geometric phase (as mentioned in the beginning of this section). Therefore, seven $|R, -l\rangle$ beams will be diverted to $\mathbf{B_{-3}} \sim \mathbf{B_{+3}}$ orders.

The phase profile for Φ_2 (Figure 2b) is chosen to be as follows:

$$\Phi_2 = \varphi_l + \varphi_D - \varphi_g \quad (2)$$

We encode Φ_2 onto the geometric metasurface MS2 (Figure 2c, green color). When the incident light is RCP, seven beams with $|L, l\rangle$ are deflected to $\mathbf{B_{-3}} \sim \mathbf{B_{+3}}$ channels because the prefactor of φ_g in Eq. (2) has opposite sign to that of Eq. (1). Similarly, when the incident light is LCP, seven $|R, -l\rangle$ beams are sent to $\mathbf{T_{-3}} \sim \mathbf{T_{+3}}$ channels.

In the next step, we merge MS1 and MS2 to form a new metasurface MS3 by selecting odd rows in MS1 and even rows in MS2, and then interleaving them with displacement D_3 (Figure 2c). We now consider the case when the incident light is linearly polarized and thus has LCP and RCP components of equal strength. Consider the $\mathbf{T_{-3}} \sim \mathbf{T_{+3}}$ channels. Each has an $|L, l\rangle$ beam and an $|R, -l\rangle$ beam generated by the blue and green nanorods, respectively, which then superpose to form a CVB. Due to the displacement D_3 between the blue and green nanorods, the phase difference δ between the $|L, l\rangle$ beam and the $|R, -l\rangle$ beam is non-zero, except for the $\mathbf{T_0}$ channel. Seven vector beam channels are therefore simultaneously generated in the top half of the observation zone ($y' > 0$ in Figure 2d). Next we consider the

$\mathbf{B}_{-3}$ ~ $\mathbf{B}_{+3}$ channels. The blue and green nanorods generate $|R,-l\rangle$ beam and $|L,l\rangle$ beam, respectively, but with a phase difference of $-\delta$. As a result, another seven CVBs will be generated in $\mathbf{B}_{-3}$ ~ $\mathbf{B}_{+3}$ channels in the bottom half of the observation zone. The relationship between the value of δ and the design parameters of the metasurface is provided in Supplementary Note 3.

We fabricate our metasurface as follows. A-Si is deposited onto a glass substrate to a thickness of 505 nm by plasma-enhanced chemical vapor deposition (PECVD). Electron beam lithography (Vistec EPBG5000+), chrome (Cr) evaporation (30 nm thick) and the lift-off process in dimethylacetamide are then performed. This yields an a-Si film on the glass substrate with a Cr hard mask. We next perform inductively-coupled reactive ion etching (ICP-RIE, Oxford Instruments PlasmaLab 100, SF_6:C_4F_8= 40sccm:90sccm) to transfer the pattern from the Cr mask to the a-Si. The Cr mask is then removed with Cr etchant. This yields an array of nanopillars, each with length ~220 nm, width ~80 nm and height ~505 nm. The pixel size is fixed at 300 nm. The metasurface has an overall extent of 600 μm × 600 μm.

For our first metasurface, we choose l=-1 for simplicity, and demonstrate its ability to generate vector beams of the same order but with varying rotation angles. It is well known that a radially polarized beam can be generated if $|L,-1\rangle$ superposes with $|R,1\rangle$, provided that δ is zero. We design our metasurface so that δ takes values of -π, -2π/3, -π/3, π/3, 2π/3 and π for $\mathbf{T}_{-3}$, $\mathbf{T}_{-2}$, $\mathbf{T}_{-1}$, $\mathbf{T}_{+1}$, $\mathbf{T}_{+2}$ and $\mathbf{T}_{+3}$ channels. The polarization distribution of these channels can be regarded as a radially polarized light that is rotated by $\delta/2$. The polarizations of channels $\mathbf{B}_{-3}$ to $\mathbf{B}_{+3}$ are the same as those of channels $\mathbf{T}_{+3}$ to $\mathbf{T}_{-3}$, respectively. A discussion (including schematic illustration) of the designed polarization distributions of the channels is provided in Supplementary Note 4. We next perform experiments to characterize the CVBs generated by the metasurface. The experimental setup we use to characterize the CVBs and scanning electron microscopy images of the metasurface are shown in Supplementary Note 5. A collimated laser diode (λ=635 nm) is used as the light source. Linearly polarized light illuminates the metasurface at normal incidence. The generated CVBs are analyzed with a rotating polarizer. Images of the light field that passes through the polarizer are captured with a charge coupled device (CCD) camera. When the transmission direction of the polarizer is along θ, the intensity of the beam in areas whose local polarization is along $\theta + 90°$ drops to zero, i.e. dark nodes can be observed. The experimentally-obtained charge coupled device (CCD) images of the different channels for different analyzer directions are shown in Figure

3. In Supplementary Note 6 we show the desired results, i.e., the images we expect to be produced when the CVBs pass through the analyzer. Comparison between Figure 3 and Supplementary Note 6 demonstrates that our experiments achieve the desired polarization states. The polarization of the CVBs changes gradually from the -3rd to +3rd channels, which is due to the diffraction-direction related phase difference δ between the LCP and RCP components. However, if we can independently control the complex amplitude (not just phase) of the LCP and RCP beams, it is possible to control the CVB states arbitrarily since we can encode arbitrary δ value to a given channel.

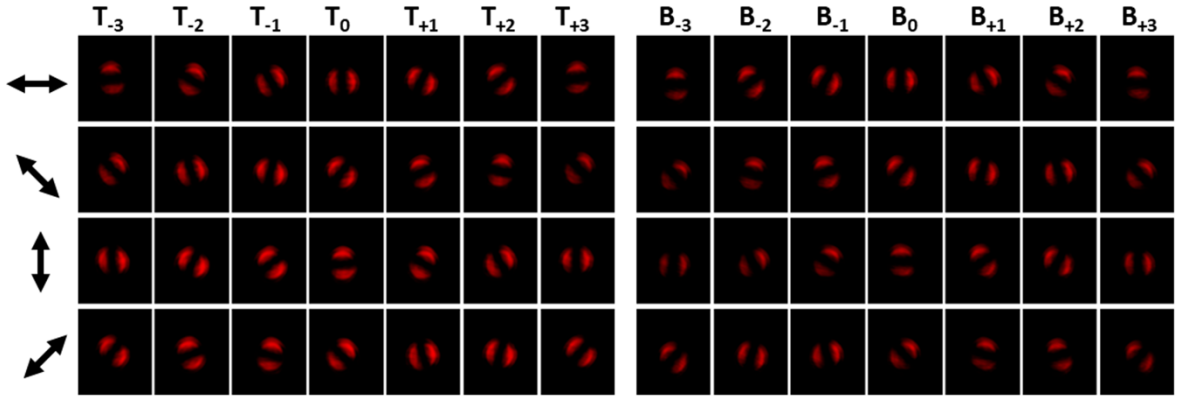

Figure 3 Experimental results obtained with the first metasurface design at a wavelength of λ=635 nm. The double-headed black arrows represent the transmission direction of the analyzing polarizer.

To show the versatility of this approach, we next produce a second metasurface that generates CVBs of different orders. We first design Φ_1' that generates 13 LCP OAM beams located at the -6th to 6th diffraction orders in the top half of the observation zone, namely $\mathbf{T_{-6}} \sim \mathbf{T_{+6}}$. The topological charge of the l^{th} order is -l. Similarly, we choose Φ_2' to generate 13 RCP OAM beams in the -6th to 6th diffraction orders in the top half of the observation zone, where the topological charge of the l^{th} order is l. Details of the design process can be found in Supplementary Note 7. We then interleave MS1 and MS2 to form MS3 (Figure 2c) with D_3 = 0. The desired polarization distributions of the CVBs of this metasurface are shown schematically in Supplementary Note 8. We fabricate and test this metasurface using the same process and experimental set-up we use for the first metasurface. The experimental results, i.e. CCD camera images of the generated CVBs are they pass through an analyzing polarizer, are shown in Figure 4. In Supplementary Note 9, we provide simulated patterns, i.e. the images that would result from passing the desired CVBs through the analyzing polarizer.

It can be seen that the experimental results are in good agreement with the simulations. This confirms that the second metasurface produces the desired CVB array. We also note the following interesting property. Let us observe the evolution of the patterns in each column of Figure 4 and compare different columns. It can be seen that the rotation speed of the patterns in the first diffraction order is l times faster than that in the l^{th} order. For example, the pattern in $\mathbf{T}_{-1}$ channel rotates by 45° as we go from the 1st row to the 2nd row in Figure 4, but rotates by 22.5° for $\mathbf{T}_{-2}$ channel. This can be understood as follows. In the first diffraction orders ($\mathbf{T}_{-1}$, $\mathbf{T}_{+1}$, $\mathbf{B}_{-1}$ and $\mathbf{B}_{+1}$ channels), the polarization direction rotates by 2π when one traverses one rotation around the central axis. This can be seen from Figure S4 of the Supplementary Note 8. From this figure, it can also be seen that for the l^{th} diffraction orders, the polarization direction rotates by $l \times 2\pi$ when traversing one rotation. This produces the aforementioned property observed in Figure 4.

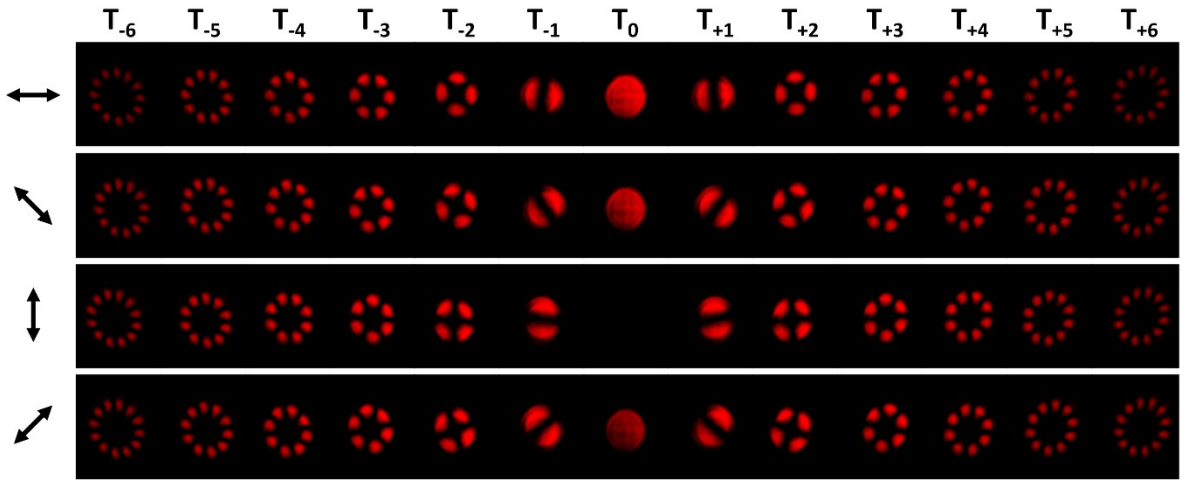

Figure 4 Experimentally obtained CCD images to verify the polarization distribution of the CVBs. Here we have 13 channels in the top half of the observation zone and 12 of them carry CVBs except for $\mathbf{T}_0$. The other 13 channels in the bottom half of the observation zone are not shown since they are the same with the top channels due to their symmetrical positions.

We now consider the efficiency of the metasurface. This is defined as the power in all the channels (including all the top channels and the bottom channels) divided by that of the incident light. To measure the efficiency, the spot size of the laser beam impinging on the metasurface is reduced by a lens (f = 20 cm) so that it is smaller than the metasurface extent. The powers of the incident light and diffraction orders are measured by a power meter (Thorlabs PM100D). The measured efficiency is 21.6% for the first metasurface and 11.8%

for the second metasurface at λ = 635 nm. The mean value and the standard deviation of the power among different orders are measured to be 13.34 μW/0.53 μW for the first metasurface, and 3.94 μW /0.64 μW for the second metasurface.

It is well known that the diffraction angles of an ordinary grating change with the wavelength of the incident light. This also occurs with our metasurfaces for the same reason. However, in our approach, the phase profile of the generated OAM beams and the phase difference δ between the LCP and RCP OAM beams are constant, i.e. do not vary with wavelength. Our metasurfaces are therefore broadband and can generate the same orthogonal vector beams regardless of the incident wavelength. To verify this point, we experimentally obtain images using lasers with a variety of wavelengths (450 nm, 532 nm and 780 nm). The results are shown in the Supplementary Note 10.

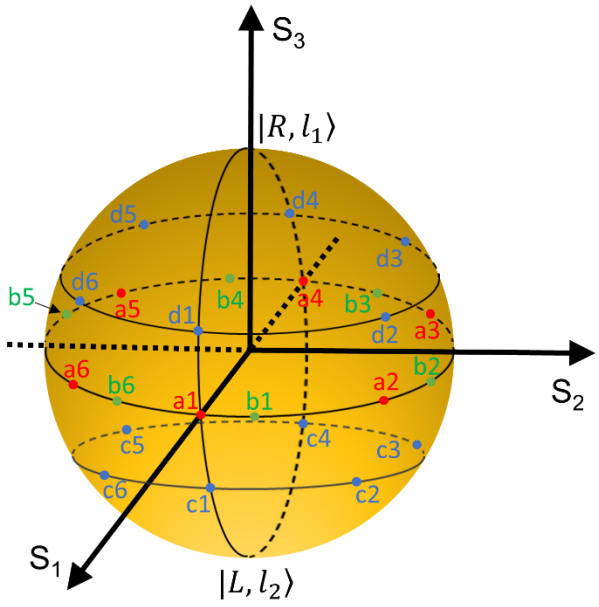

Figure 5 Representation of the vector fields in the high order Poincaré sphere (HOP).

Let us now consider the polarization states generated by the metasurfaces in more detail. It is well known that the polarization state of a beam can be represented by a point on the Poincaré sphere. However, this is only applicable for homogeneous planar waves. For CVBs, it is convenient to adopt the concept of the high order Poincaré sphere (HOP). The two poles of the HOP represent two vortex beams with orthogonal circular polarization and different topological charges, and a CVB can be represented by a point on the surface of HOP. For the first metasurface (Figure 3), these states can be represented by points a1-a6 on the surface of the high-order Poincaré sphere[13, 40] if its north and south poles represent $|R, 1\rangle$ and $|L, -1\rangle$,

respectively (Figure 5). The points a1-a6 on the HOP represent the CVBs resulting from the superposition of $|L,-1\rangle$ and $|R,1\rangle$ with phase differences δ of 0, π/3, 2π/3, π, -2π/3 and -π/3, respectively. We thus have the following. Point a1 correspond to $\mathbf{T_0}$ and $\mathbf{B_0}$ channels, a2: $\mathbf{T_{+1}}$ and $\mathbf{B_{-1}}$ channels, a3: $\mathbf{T_{+2}}$ and $\mathbf{B_{-2}}$ channels, a4: $\mathbf{T_{+3}}$, $\mathbf{T_{-3}}$, $\mathbf{B_{+3}}$, $\mathbf{B_{-3}}$ channels, a5: $\mathbf{T_{-2}}$ and $\mathbf{B_{+2}}$ channels, and a6: $\mathbf{T_{-1}}$ and $\mathbf{B_{+1}}$ channels. If we rotate the incident linearly polarized light with a half-wave plate, the phase difference δ between the LCP and RCP components of the incident light is modified. The CVBs generated by the first metasurface will thus be rotated. This changes the longitude of points a1~a6 by rotating them around the S3 axis, e.g., to b1~b6. Now consider what happens if the phase difference δ between the LCP and RCP components is unchanged, but the ratio η between the incident LCP and RCP is modified. The longitude of points a1~a6 remain the same, but their latitudes will be modified from the equator to the southern hemisphere, (e.g. c1~c6) if η>1, and to the northern hemisphere of the HOP (e.g. d1~d6) if η<1. For the second metasurface (Figure 4), we have zero horizontal displacement (D_3=0) between the two types of nanorods, and therefore we have δ=0 for all the generated CVBs. For example, the T_{+6} and B_{-6} channels of the second metasurface can be represented by the a1 point if the north and south poles of the HOP are |R,+6> and |L,-6>, respectively. Similarly, we can map CVBs of other channels to a1 (δ=0) on different types of HOPs.

3. Conclusion

We have demonstrated a method to generate multiple CVBs with different polarization states through a single metasurface. Since the LCP/RCP vortex beam array generation, polarization rotation and superposition are achieved by the same metasurface, bulky optical systems with tight alignment tolerances are avoided. We thus achieve a significant reduction in the size and complexity of systems needed for CVB generation. Each metasurface can generate CVBs over a broad wavelength range, due to its geometric phase profile and the phase difference between to the LCP and RCP vortex beams being inherently wavelength-independent. The orders of the CVBs, the rotation angles of the CVBs, and the number of channels in the CVB array can be readily altered by the design of the metasurface. The positions of the CVBs on the HOPs can be dynamically changed by tuning the polarization states of the incident light. We anticipate that the proposed device could broaden the application scope of CVBs.

Supporting Information

Supporting Information is available from the Wiley Online Library or from the author.

Acknowledgements

This work was supported in part by the Australian Research Council Centre of Excellence for Transformative Meta-Optical Systems (Project No. CE200100010). This work was performed in part at the Melbourne Centre for Nanofabrication (MCN) in the Victorian Node of the Australian National Fabrication Facility (ANFF).

Conflict of interest

The authors declare no conflict of interest.

Received: ()

Revised: ()

Published online: ()

References

[1] D. G. Hall, *Opt. Lett.* **1996**, 21, 9.
[2] Q. W. Zhan, *Opt. Lett.* **2006**, 31, 1726.
[3] M. Yoshid, Y. Kozawa, S. Sato, *Opt. Lett.* **2019**, 44, 883.
[4] B. J. Roxworthy, K. C. Toussaint, Jr., *New J. Phys.* **2010**, 12, 073012.
[5] Y. Tang, W. Perrie, D. R. Sierra, Q. Li, D. Liu, S. P. Edwardson, G. Dearden, *Micromachines* **2021**, 12, 376.
[6] Q. Zhan, *Adv. Opt. Photonics* **2009**, 1, 1.
[7] D. Pohl, *Appl. Phys. Lett.* **1972**, 20, 266.
[8] S. C. Tidwell, D. H. Ford, W. D. Kimura, *Appl. Opt.* **1990**, 29, 2234.
[9] P. Li, X. Fan, D. Wu, X. Guo, Y. Li, S. Liu, J. Zhao, *Opt Express* **2019**, 27, 30009.
[10] T. Grosjean, D. Courjon, M. Spajer, *Opt. Commun.* **2002**, 203, 1.
[11] G. Milione, M. P. J. Lavery, H. Huang, Y. X. Ren, G. D. Xie, T. A. Nguyen, E. Karimi, L. Marrucci, D. A. Nolan, R. R. Alfano, A. E. Willner, *Opt. Lett.* **2015**, 40, 1980.
[12] C. Rosales-Guzman, N. Bhebhe, A. Forbes, *Opt. Express* **2017**, 25, 25697.
[13] Y. Tang, W. Perrie, J. Schille, U. Loeschner, Q. Li, D. Liu, S. P. Edwardson, A. Forbes, G. Dearden, *J. Phys. D Appl. Phys.* **2020**, 53, 465101.
[14] N. F. Yu, P. Genevet, M. A. Kats, F. Aieta, J. P. Tetienne, F. Capasso, Z. Gaburro, *Science* **2011**, 334, 333.
[15] G. Zheng, H. Mühlenbernd, M. Kenney, G. Li, T. Zentgraf, S. Zhang, *Nat. Nanotechnol.* **2015**, 10, 308.
[16] L. Wang, S. Kruk, H. Z. Tang, T. Li, I. Kravchenko, D. N. Neshev, Y. S. Kivshar, *Optica* **2016**, 3, 1504.
[17] A. Leitis, A. Tittl, M. K. Liu, B. H. Lee, M. B. Gu, Y. S. Kivshar, H. Altug, *Sci. Adv.* **2019**, 5, aaw2871.
[18] P. X. Zheng, Q. Dai, Z. L. Li, Z. Y. Ye, J. Xiong, H. C. Liu, G. X. Zheng, S. Zhang, *Sci. Adv.* **2021**, 7, abg0363.
[19] Y. Zhou, Kravchenko, II, H. Wang, H. Y. Zheng, G. Gu, J. Valentine, *Light Sci. Appl.* **2019**, 8, 80.
[20] R. Zhao, B. Sain, Q. Wei, C. Tang, X. Li, T. Weiss, L. Huang, Y. Wang, T. Zentgraf, *Light Sci. Appl.* **2018**, 7, 90.

[21] X. Xie, M. Pu, J. Jin, M. Xu, Y. Guo, X. Li, P. Gao, X. Ma, X. Luo, *Phys. Rev. Lett.* **2021**, 126, 183902.
[22] B. Yang, D. Ma, W. Liu, D.-Y. Choi, Z. Li, H. Cheng, J. Tian, S. Chen, *Optica* **2022**, 9, 217.
[23] S. Wang, P. C. Wu, V. C. Su, Y. C. Lai, M. K. Chen, H. Y. Kuo, B. H. Chen, Y. H. Chen, T. T. Huang, J. H. Wang, R. M. Lin, C. H. Kuan, T. Li, Z. Wang, S. Zhu, D. P. Tsai, *Nat. Nanotechnol.* **2018**, 13, 227.
[24] T. Lei, M. Zhang, Y. Li, P. Jia, G. N. Liu, X. Xu, Z. Li, C. Min, J. Lin, C. Yu, H. Niu, X. Yuan, *Light Sci. Appl.* **2015**, 4, e257.
[25] W. H. Yang, S. M. Xiao, Q. H. Song, Y. L. Liu, Y. K. Wu, S. Wang, J. Yu, J. C. Han, D. P. Tsai, *Nat. Commun.* **2020**, 11.
[26] M. Lawrence, D. R. Barton, J. Dixon, J. H. Song, J. van de Groep, M. L. Brongersma, J. A. Dionne, *Nat. Nanotechnol.* **2020**, 15, 956.
[27] J. Lin, P. Genevet, M. A. Kats, N. Antoniou, F. Capasso, *Nano Lett.* **2013**, 13, 4269.
[28] J. T. Heiden, F. Ding, J. Linnet, Y. Q. Yang, J. Beermann, S. I. Bozhevolnyi, *Adv. Opt. Mater.* **2019**, 7, 1801414.
[29] J. Han, Y. Intaravanne, A. N. Ma, R. X. Wang, S. T. Li, Z. C. Li, S. Q. Chen, J. S. Li, X. Z. Chen, *Laser Photonics Rev.* **2020**, 14, 2000146.
[30] H. Chen, Z. Chen, Q. Li, H. Lv, Q. Yu, X. Yi, *J. Mod. Opt.* **2015**, 62, 638.
[31] Q. Guo, C. Schlickriede, D. Wang, H. Liu, Y. Xiang, T. Zentgraf, S. Zhang, *Opt. Express* **2017**, 25, 14300.
[32] Y. J. Bao, J. C. Ni, C. W. Qiu, *Adv. Mater.* **2020**, 32, 1905659.
[33] G. X. Li, M. Kang, S. M. Chen, S. Zhang, E. Y. B. Pun, K. W. Cheah, J. S. Li, *Nano Lett.* **2013**, 13, 4148.
[34] J.-Y. Guo, X.-K. Wang, J.-W. He, H. Zhao, S.-F. Feng, P. Han, J.-S. Ye, W.-F. Sun, G.-H. Situ, Y. Zhang, *Adv. Opt. Mater.* **2018**, 6, 1700925.
[35] Y. F. Hu, X. Liu, M. K. Jin, Y. T. Tang, X. C. Zhang, K. F. Li, Y. Zhao, G. X. Li, J. Zhou, *Photonix* **2021**, 2, 10.
[36] P. Chen, S.-J. Ge, W. Duan, B.-Y. Wei, G.-X. Cui, W. Hu, Y.-Q. Lu, *ACS Photonics* **2017**, 4, 1333.
[37] F. Yue, D. Wen, C. Zhang, B. D. Gerardot, W. Wang, S. Zhang, X. Chen, *Adv. Mater.* **2017**, 29, 1603838.
[38] E. Wang, L. Shi, J. Niu, Y. Hua, H. Li, X. Zhu, C. Xie, T. Ye, *Adv. Opt. Mater.* **2019**, 7, 1801415.
[39] Z. H. Jiang, L. Kang, T. Yue, H.-X. Xu, Y. Yang, Z. Jin, C. Yu, W. Hong, D. H. Werner, C.-W. Qiu, *Adv. Mater.* **2020**, 32, 1903983.
[40] G. Milione, H. I. Sztul, D. A. Nolan, R. R. Alfano, *Phys. Rev. Lett.* **2011**, 107, 053601.